

# On the alignment for precession electron diffraction

Yifeng Liao\*, Laurence D. Marks

Department of Materials Science and Engineering, Northwestern University, Evanston, IL 60208, United States

## ARTICLE INFO

### Article history:

Received 8 February 2012

Received in revised form

26 March 2012

Accepted 30 March 2012

Available online 7 April 2012

### Keywords:

Precession electron diffraction

CoCrMo alloy

M<sub>23</sub>C<sub>6</sub> carbide

Alignment

## ABSTRACT

Precession electron diffraction has seen a fast increase in its adoption as a technique for solving crystallographic structures as well as an alternative to conventional selected-area and converged-beam diffraction methods. One of the key issues of precession is the pivot point alignment, as a stationary apparent beam does not guarantee a fixed pivot point. A large precession tilt angle, along with pre-field and post-field misalignment, induces shift in the image plane. We point out here that the beam should be aligned to the pre-field optic axis to keep the electron illumination stationary during the rocking process. A practical alignment procedure is suggested with the focus placed on minimizing the beam wandering on the specimen, and is demonstrated for a (110)-oriented silicon single crystal and for a carbide phase (~20 nm in size) within a cast cobalt–chromium–molybdenum alloy.

© 2012 Elsevier B.V. All rights reserved.

## 1. Introduction

Determining the crystallographic structure of nanocrystallites is crucial in studying nanoparticles and fine precipitates either embedded in a matrix or on a support as in heterogeneous catalysis. X-ray diffraction analysis based on kinematical theory has been successfully developed for bulk materials at the millimeter scale, but it is hard to impossible at present for the crystals of nanometer or submicron size that materials scientists often encounter. The spatial resolution of a modern transmission electron microscope (TEM) can easily reach the atomic scale, making it ideal for probing local nanostructure. However, electron diffraction crystallography has had to wrestle with the severe problem of multiple scattering when electrons interact with matter, which makes the interpretation of the diffraction results complicated and sometimes ambiguous. Electron crystallography has become much easier since the development of precession electron diffraction (PED), invented by Vincent and Midgley in 1994 [1], in which the electron diffraction is collected with the electron beam rocking about the optical axis. The PED models [2–5] developed so far show that PED intensities are close to what one would expect based on kinematical theory when the conical semi-angle is large enough, usually greater than 20 mrad [6,7]. In fact, PED has seen increased application since a commercial product was made available on the market [2–4,6,8–17]. It has been shown that PED is a powerful tool for determining the structure of a wide range of materials, such as nano-precipitates in alloys [9,18,19] and oxides [17,20,21] ((Ga,In)<sub>2</sub>SnO<sub>5</sub> and

zeolites). In addition, Midgley et al. reported that PED can be used to determine the Debye–Waller factors of silicon, diamond, and chromium [22], whilst Avilov et al. measured the atomic bonding information of CaF<sub>2</sub> using the PED technique [23].

Despite its increasing popularity, one issue for PED is the necessary complexity of the alignment, due to the multiple large-angle beam tilts. For example, the tilt introduces additional stigmatism, which should be compensated by a three-fold stigmatism-correcting system as described previously [24,25]. While for a modern TEM the beam size, for either regular converged or parallel illumination, can be set to a few nanometers or less, the spatial resolution is limited by how well the beam stays stationary on the specimen during the rocking process, which we will call the pivot point problem. For an ideal PED system, the beam should stay still on the same area for all azimuthal angles to ensure that the collected diffracted beams at different times originate from the same area. Although this issue has been widely recognized in the literature [8,24,26,27], there has been no detailed documentation on how to obtain a fixed pivot point. In this paper we describe some alignment operations that affect the pivot point, and provide a detailed alignment procedure based upon our analysis. As shall be seen, the effort is not trivial.

## 2. Experimental

A 200 kV Jeol 2100F TEM equipped with a home-built precession electron system [27,28] was used for PED examination. Two specimens were examined: a silicon thin foil oriented along its [110] zone axis was used for calibration, and a cast cobalt–chromium–molybdenum (CoCrMo with a composition of Co–26Cr–6Mo in wt%) thin foil with nanostructured carbides was used

\* Corresponding author.

E-mail address: [yifeng-liao@northwestern.edu](mailto:yifeng-liao@northwestern.edu) (Y. Liao).

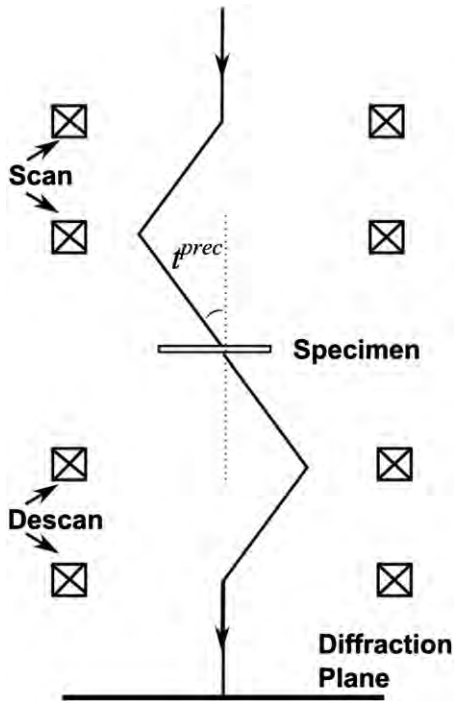


Fig. 1. Simplified ray diagram schematic of PED.

to test the spatial resolution of the PED system. The silicon foil was prepared using conventional polishing/ion milling methods, while the CoCrMo alloy, which was cut from a retrieved hip implant, was prepared using a FEI Helios dual beam focused ion beam (FIB) system. The precession semi-angle was set to a nominal 25 mrad and was determined (using the silicon diffraction pattern for calibration) to be 23.7 mrad. The misalignment between the coma-free tilt axis and the high-voltage center was about 4 mrad, and the three-fold astigmatism of the post-field was about 1  $\mu\text{m}$ .

### 2.1. Where is the beam?

Most of the misalignment and astigmatism can be minimized by conventional routine alignment procedures and we assume that the beam tilt and shift purities have been correctly set up. We focus our efforts on the consequences of the large beam tilt of the precessed beam as well as the misalignment between the pre-field and post-field optical axis.

Fig. 1 shows a simplified ray diagram for a PED system. The electron beam is bent twice by the two deflecting coils, denoted as upper scan and lower scan, respectively, before it arrives to the sample. By changing the currents of the upper and lower deflecting coils, the beam rocks conically about the pivot point. Previous studies showed that the beam tilt angle  $t^{\text{prec}}$  needs to be greater than 20 mrad to effectively suppress most of the dynamical diffraction effects. Note that  $t^{\text{prec}}$  is a function of time and varies with the phase of the rocking process. The diffracted beams are

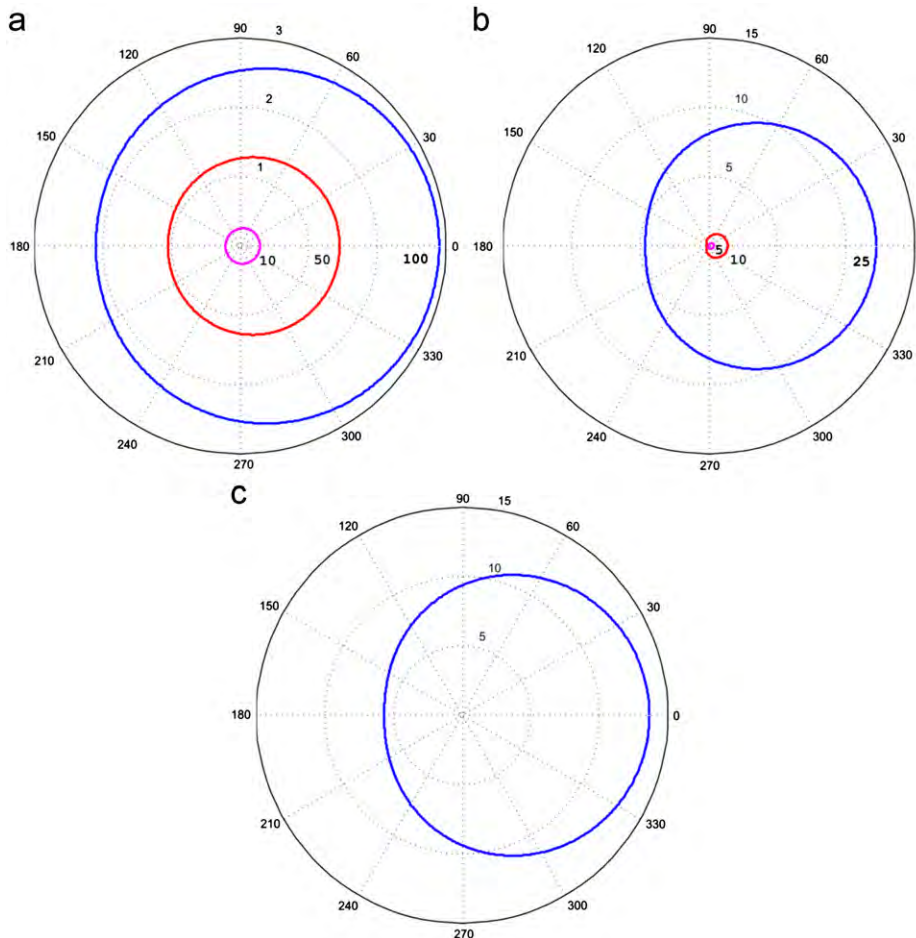


Fig. 2. (a) The influence of defocus ( $\Delta z^{\text{post}} = 10, 50, 100 \text{ nm}$ ,  $C_s^{\text{post}} = 0 \text{ mm}$ ,  $t^{\text{prec}} = 25 \text{ mrad}$ ) on apparent image shift. (b) The influence of spherical aberration ( $\Delta z^{\text{post}} = 50 \text{ nm}$ ,  $C_s^{\text{post}} = 0.5 \text{ mm}$ ,  $t^{\text{prec}} = 5, 10, 25 \text{ mrad}$ ). (c) The image shift is 15–20 nm when  $\Delta z^{\text{post}} = 50 \text{ nm}$ ,  $C_s^{\text{post}} = 0.5 \text{ mm}$ ,  $t^{\text{prec}} = 25 \text{ mrad}$ . (Unit: nm).

complementarily bent by the deflecting coils in the post-field column to form a fixed diffraction pattern.

The misalignment between the pre-field and post-field optic axis, which exists in any real TEM system, adds additional beam tilts. The shift in the image plane (denoted by  $d$ ) is given by

$$\underline{d}(\underline{t}^{Pre}) = \frac{1}{2\pi} \nabla \chi(\underline{t}^{Pre} + \underline{t}_{Err}^{Pre}) = (\underline{t}^{Pre} + \underline{t}_{Err}^{Pre}) \{ \Delta Z^{Pre} + C_s^{Pre} \lambda^2 |\underline{t}^{Pre} + \underline{t}_{Err}^{Pre}|^2 \} \quad (1)$$

where  $\underline{t}_{Err}^{Pre}$  is the error in the alignment of the pre-field, and  $\Delta Z^{Pre}$ ,  $C_s^{Pre}$  are the pre-field defocus and spherical aberration, respectively, and  $\lambda$  is the wavelength. (For simplicity we are ignoring astigmatism and higher-order aberrations which is not rigorously correct.) The shift for the post-field has exactly the same form, so the apparent shift in the observable image is

$$\begin{aligned} \underline{d}(\underline{t}^{Pre}) + \underline{d}(\underline{t}^{Post}) &= \frac{1}{2\pi} \nabla \chi(\underline{t}^{Pre} + \underline{t}_{Err}^{Pre}) + \frac{1}{2\pi} \nabla \chi(\underline{t}^{Pre} + \underline{t}_{Err}^{Post}) \\ &= (\underline{t}^{Pre} + \underline{t}_{Err}^{Pre}) \{ \Delta Z^{Pre} + C_s^{Pre} \lambda^2 |\underline{t}^{Pre} + \underline{t}_{Err}^{Pre}|^2 \} \\ &\quad + (\underline{t}^{Pre} + \underline{t}_{Err}^{Post}) \{ \Delta Z^{Post} + C_s^{Post} \lambda^2 |\underline{t}^{Pre} + \underline{t}_{Err}^{Post}|^2 \} \quad (2) \end{aligned}$$

As is well known, the pre-field and post-field displacements are additive (ignoring rotations taking place as the electrons go down the column as not important), and the pre-field and post-field defoci are partially canceling if the signs are opposite. If the errors in the pre-field and post-field alignments are minimal the displacements simplify, but there is really no reason this should be the case. In many cases PED is used for older microscopes and there is no reason why the misalignment of the pre-field and post-field ( $\underline{t}_{Err}^{Pre} - \underline{t}_{Err}^{Post}$ ) is not several mrad, as it certainly is for the

instrument used herein. To our knowledge this has not been measured or considered with PED systems to date.

The first term in the right hand side of Eq. (2) is related to the beam shift on the sample, i.e. the pivot point mentioned earlier. The second term, on the other hand, determines apparent image shift in the image plane. In practice we can align the beam to either the pre-field optic axis or the post-field optic axis; the question is which one is correct. We argue that in order for the beam to pivot on fix area, the beam needs to be aligned to the pre-field optic axis, i.e. set the first term to minimum. This will also ensure that the beam rocks symmetrically on the specimen when the two-fold and higher-order astigmatisms as well as coma are ignored. The beam, however, will unavoidably enter the post-field column with some angle off the post-field optic axis, and consequently results in apparent beam shifting during the rocking process.

The correct pre-field alignment can be obtained by watching the specimen position with respect to the beam, as opposed to the beam position on the recording media (the fluorescence screen or CCD camera). Clearly the beam should be spread out rather than converged in order to see the specimen. The beam tilt should be carefully adjusted to minimize the sample shift with respect to the beam. Once the pre-field alignment is set, the beam will rock about a fixed pivot point where the diffracted beams come from. The apparent beam, on the other hand, is expected to slightly wander around on the recording media. Fig. 2 shows the apparent image shift introduced by defocus, precession angle and post-field misalignment with the pre-field aligned; the parameters are listed in Table 1. The post-field misalignment is along  $\varphi=0^\circ$ . The system used has  $C_s^{Post} \approx 0.5\text{mm}$  and  $\underline{t}_{Err}^{Pre} = 0^\circ$ . The roles of defocus and spherical aberration are compared. The image shift caused by defocus is  $\sim 6\text{ nm}$  for  $C_s^{Post} = 0\text{mm}$ ,  $\underline{t}^{Pre} = 25\text{ mrad}$  and  $\Delta Z^{Post} = 100\text{ nm}$ , and decreases linearly with decreasing  $\Delta Z^{Post}$ , as shown in Fig. 2a. Fig. 2b shows the influence of precession angle ( $\Delta Z^{Post} = 0\text{ nm}$  and  $C_s^{Post} = 0.5\text{mm}$ ). The image shift is asymmetric and increases rapidly with increasing the precession angle. The image shift is 12–15 nm which is much greater than the

**Table 1**  
Parameter settings for Fig. 2.

	$\Delta Z^{Post}$ (nm)	$C_s^{Post}$ (mm)	$\underline{t}^{Pre}$ (mrad)
Fig. 2a	10, 50, 100	0	25
Fig. 2b	50	0.5	5, 10, 25
Fig. 2c	50	0.5	25

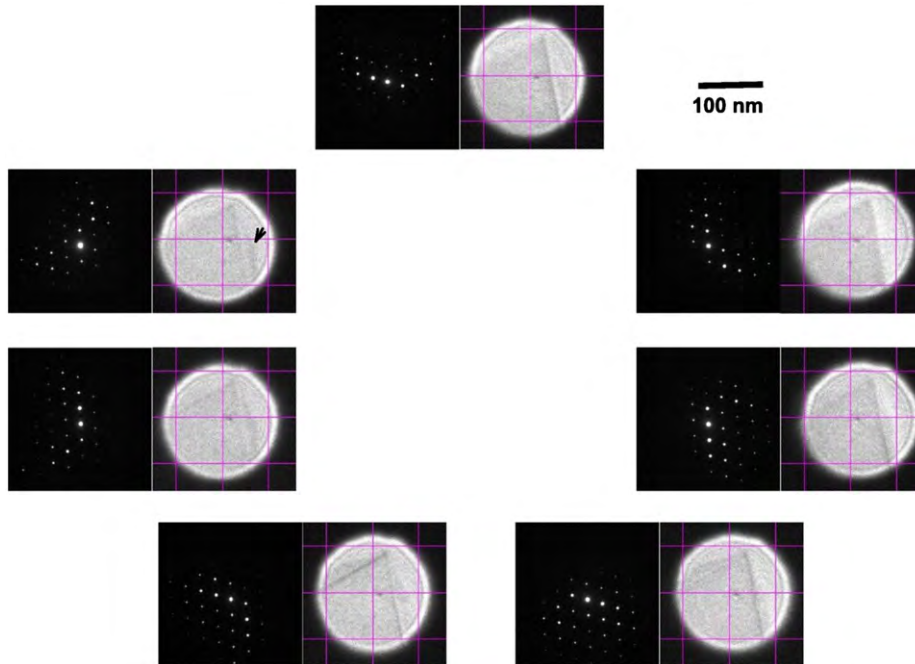


**Fig. 3.** A montage of micrographs of a silicon [110] crystal in real space during precession. Diffraction patterns with the same beam tilt conditions in the next cycle are accompanied.  $3 \times 3$  grids are plotted in each real space micrograph as reference positions. A delocalized image is arrowed.

contribution from the defocus. Fig. 2c shows the image shift for  $t_{\text{Prec}} = 25 \text{ mrad}$  and  $\Delta z^{\text{Post}} = 50 \text{ nm}$ , in which the maximum is  $\sim 20 \text{ nm}$  at  $\varphi = 90^\circ$  whilst the minimum shift of  $\sim 15 \text{ nm}$  occurs at  $\varphi = 0^\circ$ .

An aligned PED was demonstrated on the silicon [011] thin crystal and the process was recorded in both real space and reciprocal space (see the video attached in the Suppl. Info.). Fig. 3 shows a montage of seven real space images extracted from the video during a rocking cycle; the de-scan was turned off in order to obtain real space images). The edge of the specimen was examined in nano-beam mode. The corresponding nano-beam diffraction patterns recorded under the same beam tilt angles in the next rocking cycle accompany the images. We also plot  $3 \times 3$  grids in the real space images as reference positions to assist the observation of the apparent beam/sample shift. It can be seen that the sample stayed stationary rather well with respect to the beam during the rocking process. The apparent beam, on the other hand, moved around during beam precession; the shifts along the horizontal and vertical directions are  $\sim 19 \text{ nm}$  and  $\sim 16 \text{ nm}$ , respectively, which are close to what we predicted in Fig. 2c. One may also notice a clear shift of the sample edge arrowed in Fig. 3, a feature that one would expect in a PED system.

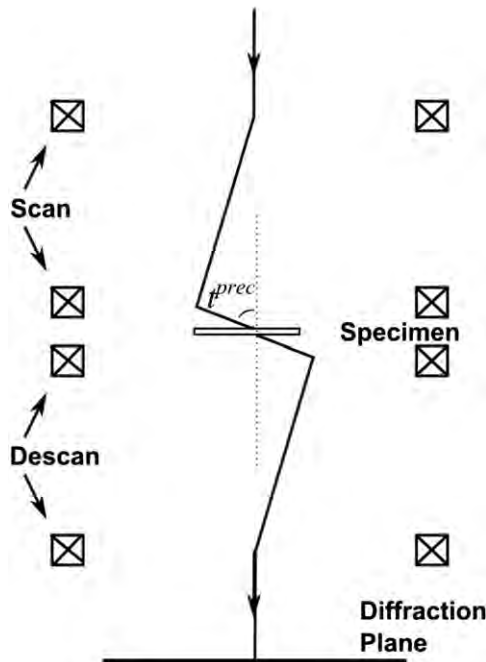


Fig. 4. A modified PED ray diagram showing the upper scan is mostly shift and the lower scan is mostly tilt.

Supplementary material related to this article can be found online at <http://dx.doi.org/10.1016/j.ultramicro.2012.03.021>.

## 2.2. Precession angle

Setting the PED alignment to the desired semi-angle ( $t_{\text{Prec}}$ ) is tricky as changing any lens current in the pre-field column results in a change in the precession angle. It is worth noting that the (conventional) ray diagram in Fig. 1, in which the beam is mirrored for the upper and lower scan, may mislead people to thinking that the beam is tilted by  $-t_{\text{Prec}}$  at the upper scan layer and is subsequently tilted by  $2t_{\text{Prec}}$  at the lower scan layer. In fact, as least for a Jeol 2100F system, the contributions of the upper/lower scanning coils to the final tilt angle are different; the upper scanning coils control mostly the beam shift, while the lower coils are mostly responsible for the beam tilt, as shown in the modified ray diagram in Fig. 4. In practice, this feature is very helpful in setting the precession angle. One only needs to set the lower scanning coil to the desired precession angle, whilst the following compensation of the upper scanning coil does not change the beam tilt much.

Once the scanning coils are set, setting the de-scan coils to bring the diffracted beams to fixed points in diffraction mode is less ambiguous, although not necessary easy. As mentioned above, beam shift/tilt operation somewhat affects both the upper and lower scanning coils; therefore, an iterative alignment is needed.

Based on the above analysis, a practical alignment procedure is suggested as the following:

- Do routine alignment including shift/tilt purities. When aligning the voltage center, the sample shift with respect to the beam should be minimal.
- Set lower scanning coil to the desired precession angle.
- Set the upper scanning coil to correct the pivot point.
- Set the de-scan coils to obtain a fixed diffraction pattern.
- Do the above alignment iteratively.

An example of setting the de-scan on the silicon thin crystal is shown in Fig. 5. Fig. 5a shows the diffraction pattern with the de-scan operation turned off. The precession semi-angle was set to  $25 \text{ mrad}$  and the real semi-angle is determined from the radius of the circle to be  $23.7 \text{ mrad}$ , an angle sufficient to obtain pseudo-kinematical diffraction [6]. Fig. 5b shows the PED pattern with the de-scan turned on, in which the intensity of the (200) diffraction spot is clearly reduced and the symmetry is well preserved.

## 2.3. PED on nanostructured carbide phases: an example

PED was also applied to recently-discovered carbide nano-phases in CoCrMo alloys that are extensively used for medical

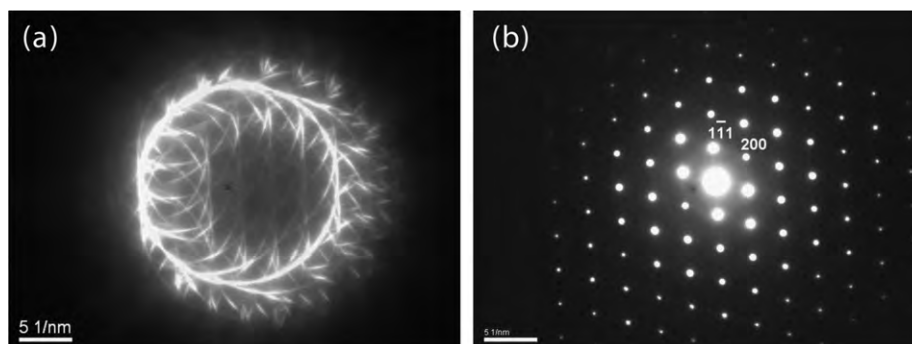
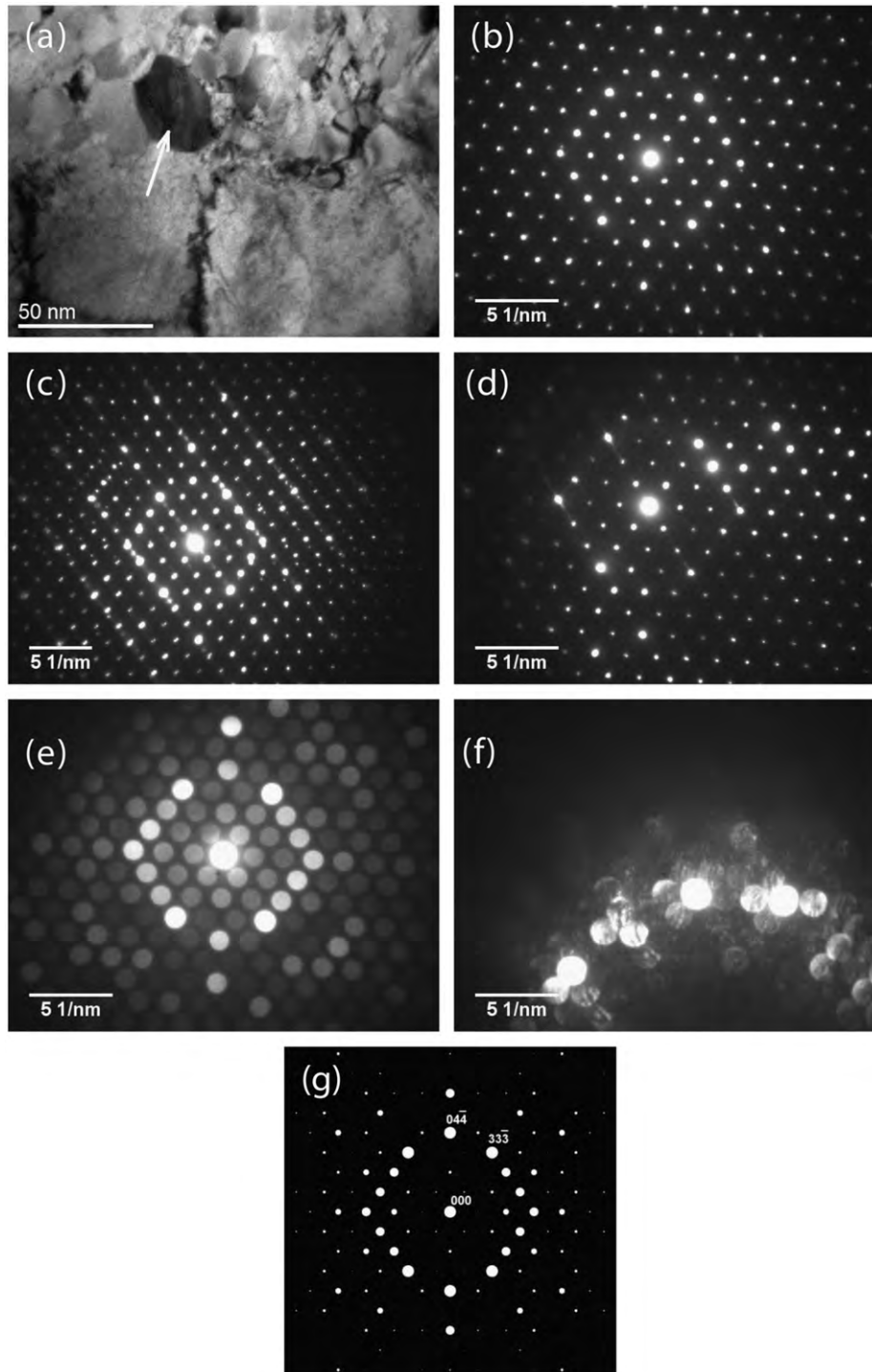


Fig. 5. (a) PED pattern of Si [011] with de-scan off. The precession semi-angle is determined from the radius of the ring to be  $23.7 \text{ mrad}$ . (b) Diffraction pattern collected with de-scan on. (200) reflection is remarkably reduced.



**Fig. 6.** An example of PED on a carbide of  $\sim 20$  nm size. (a) Bright-field micrograph showing the carbide nanostructure (arrowed). (b) PED pattern in nano-beam mode with the pre-field axis aligned. (c) PED pattern aligned using conventional method with an approximately stationary apparent beam, in which extra diffractions from adjacent phases are apparent. (d) Nano-beam diffraction with PED off for comparison. (e) CBED pattern with PED on and (f) CBED pattern with PED off. (g) Simulated pattern based on kinematical theory.

implant applications (see [29] and references therein for details). Fig. 6a shows that the carbide is composed of numerous small phases of  $\sim 20$  nm size. Fig. 6b and e shows the PED spot diffraction and CBED patterns with the pre-field axis aligned, respectively. Both nano-beam parallel illumination ( $\sim 20$  nm in diameter) and converged beam illumination were used, and in both cases the rocking electron beam was able to stay on individual nanophases. In contrast, extra diffraction spots from the adjacent phases are displayed in the PED pattern aligned

using an approximately stationary apparent beam, see Fig. 6c. The corresponding non-processed spot diffraction pattern and CBED pattern are shown for comparison in Fig. 6d and f, respectively. Fig. 6g shows a simulated diffraction pattern of  $\text{Cr}_{23}\text{C}_6$ -type carbide for the [011] zone axis based on kinematical diffraction theory. The {044} and {333} reflections are strong in the PED patterns, matching the simulated pattern very well. The symmetry of the PED pattern is well preserved even though the specimen orientation was not exactly on zone axis. The beam intensities of

the non-precessed patterns, on the other hand, are unsuitable for direct comparison because of the multiple scattering issues.

### 3. Discussion

An apparent stationary beam in PED (mostly a converged beam in the literature) on the image plane does not necessarily mean the beam is stationary on the specimen. The large precession angle, as well as the misalignment of the pre-field and the post-field, leads to shifts. The correct way to find a fixed pivot point is to spread the beam and watch the sample position with respect to the beam. The key is to align the beam with the pre-field optic axis. One would expect slight motion of the apparent beam when the pivot point is correctly set up on the specimen. As expected the spherical aberration dominates the shifts, which increases cubically with the precession angle; the defocus contributes to the shift in a linear fashion.

There are several ways to reduce the shifts due to the large tilt based on Eq. (2). First, one can set the specimen in focus, which is common practice. Secondly a  $C_s$ -corrected TEM will eliminate the shift caused by the spherical aberration. This is, however, less accessible to most labs. It would be very interesting to perform PED on a scanning transmission electron microscope (STEM), in which the pre-field optic is specifically aligned and the post-field alignment is mostly irrelevant, i.e.  $t_{Err}^{Post} = 0$ . This could significantly reduce the second term in Eq. (2). With the fine spot control in a modern STEM, PED could potentially provide pseudo-kinematical diffraction at the atomic level. We suspect that STEM mode is in general the correct way to do PED. In fact, Granesh et al. suggested incorporation of PED in diffraction STEM (D-STEM), an emerging technique that acquires diffraction patterns using a scanning electron beam, to improve the quality of the diffraction patterns in STEM mode [30].

### 4. Conclusions

We have shown that finding the pivot point by aligning the pre-field axis is essential for PED. The apparent electron beam may shift on the image plane due to both the large precession tilt and the misalignment between the pre-field and the post-field. A detailed alignment procedure is suggested. PED was successfully used to identify ~20 nm-large carbide nanostructure in a CoCrMo alloy.

### Acknowledgments

This research is supported by the NSF on Grant number CMMI-1030703 and by the NIH on Grant number 1RC2AR058993-01. The authors are indebted to Mr. Yuyuan Lin for helpful discussions and for providing the post-field misalignment angle.

### References

- [1] R. Vincent, P.A. Midgley, Double conical beam-rocking system for measurement of integrated electron diffraction intensities, *Ultramicroscopy* 53 (1994) 271–282.
- [2] K. Gjonnes, On the integration of electron diffraction intensities in the Vincent–Midgley precession technique, *Ultramicroscopy* 69 (1997) 1–11.
- [3] K. Gjonnes, Y.F. Cheng, B.S. Berg, V. Hansen, Corrections for multiple scattering in integrated electron diffraction intensities. Application to determination of structure factors in the [001] projection of Al<sub>2</sub>Fe, *Acta Crystallographica Section A* 54 (1998) 102–119.
- [4] C.S. Own, L.D. Marks, W. Sinkler, Precession electron diffraction, 1: multislice simulation, *Acta Crystallographica Section A* 62 (2006) 434–443.
- [5] P. Oleynikov, S. Hovmoller, X.D. Zou, Precession electron diffraction: observed and calculated intensities, *Ultramicroscopy* 107 (2007) 523–533.
- [6] J. Ciston, B. Deng, L.D. Marks, C.S. Own, W. Sinkler, A quantitative analysis of the cone-angle dependence in precession electron diffraction, *Ultramicroscopy* 108 (2008) 514–522.
- [7] W. Sinkler, C.S. Own, L.D. Marks, Application of a 2-beam model for improving the structure factors from precession electron diffraction intensities, *Ultramicroscopy* 107 (2007) 543–550.
- [8] B.S. Berg, V. Hansen, P.A. Midgley, J. Gjonnes, Measurement of three-dimensional intensity data in electron diffraction by the precession technique, *Ultramicroscopy* 74 (1998) 147–157.
- [9] J. Gjonnes, V. Hansen, A. Kverneland, The precession technique in electron diffraction and its application to structure determination of nano-size precipitates in alloys, *Microscopy and Microanalysis* 10 (2004) 16–20.
- [10] W. Sinkler, L.D. Marks, Characteristics of precession electron diffraction intensities from dynamical simulations, *Zeitschrift fur Kristallographie* 225 (2010) 47–55.
- [11] E.F. Rauch, J. Portillo, S. Nicolopoulos, D. Bultreys, S. Rouvimov, P. Moeck, Automated nanocrystal orientation and phase mapping in the transmission electron microscope on the basis of precession electron diffraction, *Zeitschrift fur Kristallographie* 225 (2010) 103–109.
- [12] P. Moeck, S. Rouvimov, Precession electron diffraction and its advantages for structural fingerprinting in the transmission electron microscope, *Zeitschrift fur Kristallographie* 225 (2010) 110–124.
- [13] J. Hadermann, A.M. Abakumov, A.A. Tsirlin, V.P. Filonenko, J. Gonnissen, H.Y. Tan, J. Verbeeck, M. Gemmi, E.V. Antipov, H. Rosner, Direct space structure solution from precession electron diffraction data: resolving heavy and light scatterers in Pb<sub>13</sub>Mn<sub>9</sub>O<sub>25</sub>, *Ultramicroscopy* 110 (2010) 881–890.
- [14] M. Gemmi, H. Klein, A. Rageau, P. Strobel, F. Le Cras, Structure solution of the new titanate Li<sub>4</sub>Ti<sub>8</sub>Ni<sub>3</sub>O<sub>21</sub> using precession electron diffraction, *Acta Crystallographica Section B* 66 (2010) 60–68.
- [15] W. Sinkler, C.S. Own, J. Ciston, L.D. Marks, Statistical treatment of precession electron diffraction data with principal components analysis, *Microscopy and Microanalysis (Supplement 2, Proceedings)* 13 (2007) 954CD–955CD.
- [16] J. Gjonnes, V. Hansen, B.S. Berg, P. Runde, Y.F. Cheng, K. Gjonnes, D.L. Dorset, C.J. Gilmore, Structure model for the phase Al<sub>2</sub>Fe derived from three-dimensional electron diffraction intensity data collected by a precession technique: comparison with convergent-beam diffraction, *Acta Crystallographica Section A* 54 (1998) 306–319.
- [17] C.S. Own, W. Sinkler, L.D. Marks, Rapid structure determination of a metal oxide from pseudo-kinematical electron diffraction data, *Ultramicroscopy* 106 (2006) 114–122.
- [18] A. Kverneland, V. Hansen, R. Vincent, K. Gjonnes, J. Gjonnes, Structure analysis of embedded nano-sized particles by precession electron diffraction. eta 'precipitate in an Al–Zn–Mg alloy as example, *Ultramicroscopy* 106 (2006) 492–502.
- [19] A. Kverneland, V. Hansen, G. Thorkildsen, H.B. Larsen, P. Pattison, X.Z. Li, J. Gjonnes, Transformations and structures in the Al–Zn–Mg alloy system: a diffraction study using synchrotron radiation and electron precession, *Materials Science and Engineering A* 528 (2011) 880–887.
- [20] E. Mugnaioli, T. Gorelik, U. Kolb, “Ab initio” structure solution from electron diffraction data obtained by a combination of automated diffraction tomography and precession technique, *Ultramicroscopy* 109 (2009) 758–765.
- [21] C.S. Own, A.K. Subramanian, L.D. Marks, Quantitative analyses of precession diffraction data for a large celoxide, *Microscopy and Microanalysis* 10 (2004) 96–104.
- [22] P.A. Midgley, M.E. Sleight, M. Saunders, R. Vincent, Measurement of Debye–Waller factors by electron precession, *Ultramicroscopy* 75 (1998) 61–67.
- [23] A. Avilov, K. Kuligin, S. Nicolopoulos, M. Nickolskiy, K. Boulahya, J. Portillo, G. Lepeshov, B. Sobolev, J.P. Collette, N. Martin, A.C. Robins, P. Fischione, Precession technique and electron diffractometry as new tools for crystal structure analysis and chemical bonding determination, *Ultramicroscopy* 107 (2007) 431–444.
- [24] C.S. Own, N. Dellby, O.L. Krivanek, L.D. Marks, M. Murfitt, Aberration-corrected precession electron diffraction, *Microscopy and Microanalysis* 13 (2007) 96–97.
- [25] C.S. Own, W. Sinkler, L.D. Marks, Prospects for aberration corrected electron precession, *Ultramicroscopy* 107 (2007) 534–542.
- [26] D.L. Zhang, D. Gruner, P. Oleynikov, W. Wan, S. Hovmoller, X.D. Zou, Precession electron diffraction using a digital sampling method, *Ultramicroscopy* 111 (2010) 47–55.
- [27] C.S. Own, L.D. Marks, W. Sinkler, Electron precession: a guide for implementation, *Review of Scientific Instruments* 76 (2005) 003703-1–003703-13.
- [28] C.S. Own, System Design and Verification of the Precession Electron Diffraction Technique, Department of Materials Science and Engineering, Northwestern, Evanston, 2005 (p. 161).
- [29] Y. Liao, R. Pourzal, M.A. Wimmer, J.J. Jacobs, A. Fischer, L.D. Marks, Graphitic tribological layers in metal-on-metal hip replacements, *Science* 334 (2011) 1687–1690.
- [30] K.J. Ganesh, M. Kawasaki, J.P. Zhou, P.J. Ferreira, D-STEM: a parallel electron diffraction technique applied to nanomaterials, *Microscopy and Microanalysis* 16 (2010) 614–621.